Electronic, mechanical, optical and piezoelectric properties of glass like sodium silicate (Na_2SiO_3) under compressive pressure

R. Zosiamliana,[a,b] Lalrinkima,[a,b] B. Chettri,[a,c] G. Abdurakhmanov,[d,e] M. P. Ghimire,[f,g,†] and D. P. Rai[a,*]

Received Xth XXXXXXXXXX 20XX, Accepted Xth XXXXXXXXX 20XX
First published on the web Xth XXXXXXXXXX 200X
DOI: 10.1039/b000000x

Structural, mechanical, electronic, optical and piezoelectric properties of Na_2SiO_3 are studied under different compressive unidirectional pressure(0-50 GPa with a difference of 10 GPa) using density functional theory (DFT). The calculated structural properties are well agreed with the previously reported results. At 12 GPa, our calculation shows structural phase transition from orthorhombic C$mc2_1$ to triclinic P1. The mechanical profile of Na_2SiO_3 structures under different compressive unidirectional pressures are analysed by calculating the elastic moduli, Poisson's ratio and eigenvalues of stiffness matrix. Our study shows mechanical stability of the system till pressure reaches 40 GPa. Herein, we have obtained an indirect band gap of 2.97 eV at 0 GPa. Between 0-50 GPa, the band gaps are within the range of 2.62 to 3.46 eV. The system under our study possesses wide band gap and high optical absorption in UV-Vis range of electro-magnetic(em) radiation. The calculated static refractive indices $\eta^{x,y,z}(0)$ are closed to unity suggesting its transparent behaviour. For piezoelectric properties, we have reported the total Cartesian polarization. Our calculations have revealed that Na_2SiO_3 to be one of the promising candidates for opto-electronic devices while its application in ferroelectric and piezoelectric devices could be improved with further research.

1 Introduction

A theoretical and experimental insight into a novel silica (SiO_2) based glasses have became an interesting topic among the researchers due to the presence of their wide-direct bandgap, high thermodynamical stability, low thermal conductivity and abundant in nature.[1,2] Its flexibility and reliability towards different appliances for different task has made them one of the prominent candidates in technological and commercial applications, such as battery and storage systems, fireproof fabrics, fiber optics, bio-active glasses for antibiotic-free antibacterial materials, optoelectronic devices, etc.[3–7] Moreover, modifications of such properties upon the manufacturing processes, chemical compositions thereby enhancing its resistivity towards thermal, chemical, pressure, and its transparency have made silicate glasses a promising material over wide range of applications.[8–11] Most of the important glasses are silicate glass based on the compound silica (SiO_2) or quartz.[12] The structure of silicate glass was thought to be well understood at a local level. Randall *et al.*[13] have performed the experimental investigation by using X-ray diffraction and reported that the vitreous silica probably consists of small crystals of cristobalite[13]. A later studies on silica (SiO_2) by Zachariasen *et al.*[14] reported that the heat-treated specimens occurred in vitreous forms and showed the relative orientation of two neighbouring oxygen tetrahedral. It has also been reported that the silicon atoms surrounded by oxygen may vary within a wide limit and oxygen to oxygen bond angle varies throughout the whole network.[14,15] This leads to more complications while investigating the structure of silicate glass.

The pure silica is a three dimensional network of [SiO_4] tetrahedral arranged in such a way that the silicon atom is bonded to four neighbouring oxygen atoms and which in turn each oxygen atom is bonded to two silicon atoms.[16] The structure is well described by the continuous random network (CRN).[14] Addition of alkali Na^+ cations disrupt the Si-O-Si bridging bonds (BO) that results in the formation of non-bridging oxygen (NBO) consisting of one half of the permanent broken oxygen bond. The Na^+ ions proceed close to the NBO forming weak ionic bonds producing the formation of glass-like sodium metasilicate (SiO_2+$Na_2O \rightarrow Na_2SiO_3$, ΔH^{773K} = -235 kJ mol^{-1}).[17,18] Alkali silicate are the most studied glass materials due to their important chemical and

[a] *Department of Physics, Physical Sciences Research Center (PSRC), Pachhunga University College, Mizoram University, Aizawl-796001, India*, *Email:*dibya@pucollege.edu.in*
[b] *Department of Physics, Mizoram University, Aizawl-796004, India*
[c] *Department of Physics, North-Eastern Hill University, Shillong-793022, Meghalaya, India*
[d] *Tashkent State Technical University, Tashkent, 100095 Uzbekistan*
[e] *National University of Uzbekistan, Tashkent, 100174 Uzbekistanc*
[f] *Central Department of Physics, Tribhuvan University, Kirtipur 44613, Kathmandu, Nepal*, †Email:*madhav.ghimire@cdp.tu.edu.np*
[g] *Condensed Matter Physics Research Center, Butwal 32907, Rupandehi, Nepal*

physical properties which make them relevant materials in science and technology. From some decades back, the structure, mechanical and electronic properties of glass-like sodium silicate are being investigated through experiment as well as from the computational simulation methods. The pioneer work of Grund and Pizy[19] for the structural investigation of sodium metasilicate (Na_2SiO_3) where the atomic positions had been determined from Patterson and Fourier-Bragg projections[20] and noted that the structure showed pseudo-hexagonal symmetry: later refined by Richet *et al.*[21] via Raman spectroscopy and X-ray diffraction. More recently, an experimental investigation using single-energy Raman spectroscopy and energy-dispersive X-ray powder diffraction revealed that a structural phase transition from the orthorhombic C$mc2_1$ (space group) to the lower primitive symmetry space group at 850K.[21]

Experimentally, different techniques and approaches have been implemented: the Raman spectroscopy, x-ray diffraction(XRD), nuclear magnetic resonance (NMR), x-ray absorption fine structure and extended x-ray absorption fine structure (XAFS and EXAFS) are the superlative experimental set up for structural determination and properties study.[22–31] However, Na_2SiO_3 lacks the long-range order (LRO) or transitional periodicity that forces upon complication inducing to much more challenging than in crystalline solids while inquiring structural properties.[32] To generate useful data and necessary information, reverse Monte Carlo and *Ab initio* molecular dynamics (AIMD) based on the Density functional theory (DFT) are the most preferable simulation methods.[33–35] The computational DFT base AIMD being an accurate interatomic potential has become the major appliance to probe the details of amorphous solids which is generally controlled by short-range order (SRO) and medium range order (MRO) in their structure.[36]

As far as we are aware, among the surveyed literature the theoretical and the experimental works are mainly focused on the structural and electronic properties of the Sodium Silicate (Na_2SiO_3). So, in this work in addition to the structural and electronic properties of the Sodium Silicate (Na_2SiO_3), we have also given emphasised on the unexplored properties like phase-transition, optical and piezoelectric properties under different unidirectional compressive pressures within the frame work of density functional theory (DFT).

2 Computational Details

All the calculations were performed using the density functional theory. Linear combination of atomic orbital method (LCAO) employed in QuantumATK Q-2019.12 was adopted for all DFT calculations.[37–39] For treating all electrons, an exchange-correlation functional of generalized gradient approximation(GGA) within Perdew-Burke-Ernzerhof(PBE) scheme is adopted.[40] Our sodium silicate unit cell consists of 24 atoms with 8-sodium, 4-silicon and 12-oxygen atoms. The space group of the $Na_8Si_4O_{12}$ is C$mc2_1$ or C_{2v} [12]. We have employed force field method with Limited-memory Broyden-Fletcher-Goldfarb-Shanno (LBFGS) algorithm in couple with the ReaxFF_CHOSiNa_2018 and Pedone_LiNaKSiO_2007 potentials for the geometry optimization.[41–43] These force field potentials are specially designed for alkali silicates and vastly used for its property calculations. The minimum criteria for Hellmann-Feynman force and stress tolerances were set to 0.01 eV/Åand 0.0001 eV/Å^3, respectively for geometry optimization. During geometry optimization, no constraint were imposed on the structure along any axes. The pseudojo pseudopotential of Na, Si and O considering medium basis set (similar to double zeta polarized) is used for our calculation.[44] The density mesh cut off were set to 125.0 Ha. The self-consistent field(SCF) tolerance were set to 10^{-5} Ha. The above mentioned geometry convergence criteria were followed for all the structures under a compressive stress of 0-50 GPa with a difference of 10 GPa. Monkhorst-pack method was used to sample the K-points[45] within a first Brillouin zone. For all the electronic properties calculation 5×3×6 K-points were sampled. Moreover, for partial density of states and optical calculation a high k-mesh of 8×5×10 has been taken into consideration.

3 Result and Discussion

3.1 Structural Properties

In this section, we have discussed about the structural properties of the sodium silicate. The unit cell of $Na_8Si_4O_{12}$ exists in orthorhombic crystal structure with a space group C$mc2_1$. This is to be noted that for the convenience of our calculation we have swapped the x and z axis (a↔c) and applied the unidirectional compressive pressure along the longer axis (z-axis). The optimised lattice parameters are a=6.158 Å, b=4.876 Å, c=10.630 Å. The optimised volume(V) of the unit cell is found to be 319.20 Å^3. The optimised lattice parameters (a,b,c in Å unit) versus energy (in eV) are presented in Fig.2. Table 1 shows the agreement between our results and the previously calculated results from Cuautli *et al.*[46] using PBE as exchange-correlation functionals. Our calculated volume is 2.04% and 3.95% higher than the volume calculated by using Becke, 3-parameter, Lee–Yang–Parr(B3LYP) functional by Belmonte *et al.*[47] and the one experimentally obtained by McDonald *et al.*[48], respectively. The difference in volume is due to the well-known effect of the generalized gradient approximation(GGA) exchange-correlation functionals by PBE.

The change in lattice parameters under unidirectional compressive pressure in the pressure range 0→50 GPa are reported

in Table 2. The current work gives a thorough study of the structural deformation under the unidirectional compressive pressure (0-50 GPa). However, we do not have sufficient experimental or theoretical data to compare the results of pressure related studies particularly on Na_2SiO_3. With the increased in pressure, the negative deformation along the lattice constant 'Δ c' and the positive one along 'Δ a' and 'Δ b' indicates compression and tensile strain, respectively [see Table 2]. On application of compressive pressure the change in lattice parameter 'c' is high as compared to 'a' and 'b' due to the unconstrained x and y axes as a result the dissipation of tensile stress took place along x- and y-axis. This specifies that our compressive pressure is unidirectional which is acted along the lattice parameter 'c'. The structural deformations at different pressure had led to change in the optimised unit cell volumes as: at P=0, 10, 20, 30, 40, 50 (in GPa), V=319.2, 328.5, 319.4, 311, 305.1, 301.6 (in Å^3), respectively.

The hallmarks of Na_2SiO_3 structure are the presence of [SiO_4] tetrahedral chains and that of the existence of BO and the NBO bonds where the sodium atoms are attached. The presence of NBOs in the structure make a large distortion on the tetrahedral [SiO_4] units.[18] Initially, at 0 GPa pressure, our Na_2SiO_3 existed as an orthorhombic crystal structure with a space group of C$mc2_1$. As shown in Fig. 1, Na_2SiO_3 experienced a structural phase transition from orthorhombic C$mc2_1$ space group to the lower primitive symmetry of triclinic crystal structure with space group P1 at 12 GPa.

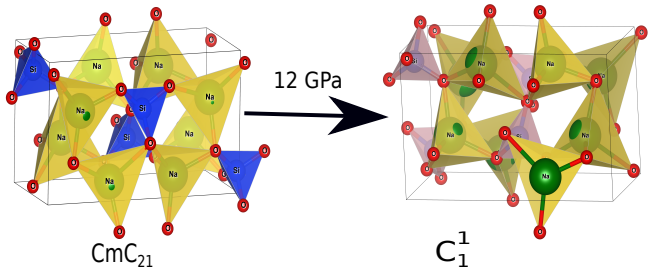

Fig. 1 Phase transition from Cmc2$_1$ $\rightarrow$ C$_1^1$ under 12 GPa unidirectional compressive pressure.

Table 1 Calculated optimised lattice parameters of Na_2SiO_3 compared to B3LYP (Belmonte *et al.*[47]), PBE (Cuautli *et al.*[46]) and Experimental (McDonald *et al.*[48]). [Swapped x and z axis (a↔c)]

Parameters	PBE-GGA (This work)	B3LYP[47]	PBE[46]	Exp.[48]
a(Å)	6.158	6.0977	6.16	6.07
b(Å)	4.876	4.8523	4.88	4.82
c(Å)	10.630	10.5676	10.63	10.48
V(Å^3)	319.20	312.673	319.546	306.6

Table 2 Calculated lattice parameters in Å and the change in lattice parameters with respect to pistine one in Å under different unidirectional pressure in GPa. [Swapped x and z axis (a↔c)]

P	a	b	c	Δa	Δb	Δc
0	6.158	4.876	10.630	0	0	0
10	6.157	5.221	10.22	-0.001	0.345	-0.41
12	6.198	5.233	10.08	0.040	0.357	-0.55
20	6.326	5.276	9.569	0.168	0.400	-1.061
30	6.446	5.316	9.077	0.288	0.440	-1.553
40	6.531	5.348	8.736	0.373	0.472	-1.894
50	6.588	5.388	8.497	0.430	0.512	-2.133

3.2 Mechanical Properties

This section is about the discussion of the mechanical properties of Na_2SiO_3. In order to perceive whether our compound meets the required stability and durability for practical applications, knowledge of its mechanical and elastic properties are essential. We have calculated the elastic constants and other mechanical properties for Na_2SiO_3 under different compressive unidirectional pressure. Our calculated elastic constants (as shown in Table 3) and the elastic constants calculated by Belmonte *et al.*[47] (using LCAO DFT/B3LYP functionals) had shown different values due to the difference in the exchange-correlation functionals employed. However, the two results had satisfied the necessary and sufficient Born criteria of mechanical stability for an orthorhombic system[49]:

$$\begin{aligned} C_{11} > 0, C_{11}C_{22} > {C_{12}}^2, \\ [C_{11}C_{22}C_{33}+2C_{12}C_{13}C_{23}-C_{11}{C_{23}}^2-C_{22}{C_{13}}^2-C_{33}{C_{12}}^2] > 0, \\ C_{44} > 0, C_{55} > 0, C_{66} > 0 \end{aligned} \quad (1)$$

From Table 3, it can be seen that the stability criteria for orthorhombic system are satisfied at 0 and 10 GPa pressures showing the mechanical stabiliy of the orthorhombic phase of Na_2SiO_3. In the previous sub-section, we have reported that there is a phase transition from orthorhombic C$mc2_1$ to triclinic P1 at 12 GPa pressure. Further, for triclinic system the Born criteria of mechanical stability are[49,50]:

$$\begin{aligned} C_{11} > 0, C_{22} > 0, C_{33} > 0, C_{44} > 0, C_{55} > 0, C_{66} > 0, \\ [C_{11}+C_{22}+C_{33}+2(C_{12}+C_{13}+C_{23})] > 0, C_{33}C_{55}-{C_{35}}^2 > 0, \\ C_{44}C_{66}-{C_{46}}^2 > 0, C_{22}+C_{33}-2C_{23} > 0 \end{aligned} \quad (2)$$

Our calculated elastic constants in the pressure range of 12-50 GPa (as shown in Table 3) had satisfied the above mentioned mechanical stability criteria for triclinic phase of Na_2SiO_3. The agreement of the stability criteria had shown that our system Na_2SiO_3 is mechanically stable at the different compressive pressure ranges of 0-50 GPa. This is also confirmed by

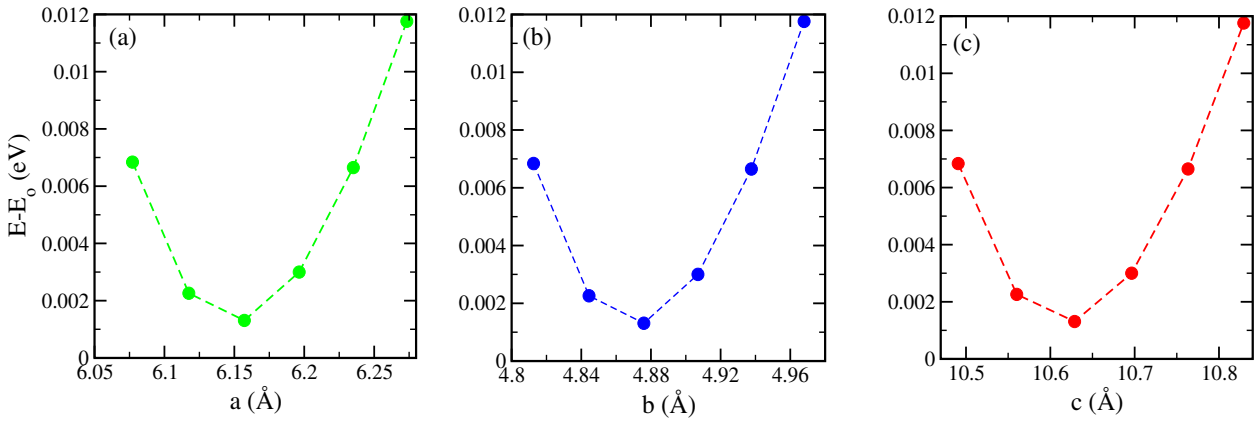

Fig. 2 Difference of energy (E-E$_o$) eV as a function of Lattice constants of Na_2SiO_3 (a) a (Å), (b) b (Å) and (c) c (Å) (E$_o$ is the minimum ground state energy).

the fact that the stiffness matrix is positive at all pressures except at P=50 GPa as can be seen in the eigenvalues reported in Table 5. At 50 GPa there is a mismatching between the Born criteria for mechanical stability and the stiffness matrix eigenvalues where we get negative value at λ_1. Mouhat *et al.*[49] had reported that when studying such low-symmetry crystals like monoclinic and triclinic, it was usually more convenient to keep the stiffness coefficients in matrix form and check whether all eigenvalues of C were positive. In Fig. 3, we have presented the calculated phonon dispersion curves of Na_2SiO_3 to test its dynamical stability between 0-50 GPa. Since, the unit cell consists of 24 atoms hence, there are 72 branches in the phonon dispersion curve. At 0 and 30 GPa [see Fig. 3(a and d)] we observe positive phonon spectrum, this implies that Na_2SiO_3 is dynamically stable at these pressures. However, at 10, 20, 40 and 50 GPa [see Fig. 3(b,c,e and f)] we obtain small negative phonon spectrum of the considered system which could be highly probable that it is just a numerical noise in the calculation as the lowest phonon curve does not cross the energy values of -10 meV for all four cases. This implies that the considered system i.e., Na_2SiO_3 is dynamically stable between the applied mechanical stress of 0-50 GPa. From Table 3, it is obvious that between P=10-40 GPa our calculated C_{11}, C_{22}, C_{33} are considerably larger than C_{66}, C_{55}, C_{44} which shows that Na_2SiO_3 has more resistance to axial compression as compared to shear deformation. This can be confirmed by comparing the bulk modulus and shear modulus reported in Table 4. From the analysis of our calculated elastic constants (C_{ij}), it can be seen that C_{11} and C_{22} decreases while C_{55} increases when pressure escalates from 10 GPa to 12 GPa, this suggest that there is a tendency of phase transition from orthorhombic C$mc2_1$ to lower symmetry phase (see Fig. 1).
In Table 4, the calculated elastic moduli and the Poisson's ratio under different compressive pressures are reported. Our reported bulk modulus(B), Young's modulus(Y) and shear modulus(G) are estimated in Voigt (uniform strain assumption)[51], Reuss (uniform stress assumption)[52] and Hill assumption.[53] It can be seen that there are regular or low fluctuation in our calculated elastic moduli from 0-40 GPa pressures indicating that our system is mechanically stable. At P=50 GPa, the elastic moduli fluctuate very high or our calculated elastic moduli are out of order compared to lower pressures (i.e. 0-40 GPa) , which might be due to the fact that our system (Na_2SiO_3) shows mechanical unstablility at 50 GPa. Glass-like Na_2SiO_3 materials are usually brittle.[54] The brittleness or ductility is generally characterized by the values of Poisson's ratio. We have reported our calculated Poisson's ratio (ν) estimated using the Voigt, Reuss and Hill assumptions. From Table 4, it is obvious that the value of ν is increasing with pressure showing that Na_2SiO_3 becomes more ductile with pressure. Interestingly, between 0-40 GPa, one can find that our system undergoes tensile deformation which can be confirmed by the fact that all the Poisson's ratio are positive between this range of pressure. However, at 50 GPa, the value of ν_H drastically falls to negative. This negative Poisson's ratio (at ν_H=-34.603, see Table 4) has resulted in compressive deformation. Thus, at 50 GPa Na_2SiO_3 shows the property of auxetic materials which are having high applications in biomedical field, surgical implants and even for piezoelectric sensors and actuators.[55–58]

3.3 Electronic Properties

The most fundamental property while investigating the atomic level interaction in any material is the electronic property. In this section, we present detail results of electronic properties for pristine Na_2SiO_3(0 Gpa) and Na_2SiO_3 at five different pressures. Figure 4 and 5 show the calculated electronic band structure and partial density of state (PDOS) for Na_2SiO_3. It is found that the top of the valence bands (VBs) have small

Table 3 Calculated elastic constants C_{ij} under different unidirectional pressure (both in GPa units). Here, at 0 and 10 GPa Na_2SiO_3 is of orthorhombic ($Cmc2_1$) phase and between 12-50 GPa Na_2SiO_3 is at triclinic (P1) phase.

P	C_{11}	C_{22}	C_{33}	C_{44}	C_{55}	C_{66}	C_{12}	C_{13}	C_{23}	C_{35}	C_{46}	C_{15}	C_{25}
0	57.36	43.76	59.70	24.32	51.91	27.74	43.47	19.38	10.51	-	-	-	-
10	52.60	157.37	111.47	38.05	21.60	50.56	29.81	34.62	42.08	-	-	-	-
12	45.27	154.18	135.71	36.35	26.58	48.35	34.21	43.54	53.20	-11.11	-9.94	-5.28	-6.08
20	80.36	179.37	188.73	27.41	18.38	55.80	53.81	45.66	60.86	-2.28	-2.62	-8.08	-4.58
30	118.92	189.26	196.31	20.92	16.46	59.71	71.84	58.66	62.90	1.24	-1.68	-2.48	-0.31
40	131.05	180.53	207.47	17.47	16.62	62.87	71.60	66.00	68.26	0.36	-0.82	-2.66	-1.47
50	5.25	180.28	169.59	22.00	30.47	53.31	19.14	41.27	57.20	5.05	5.32	-28.00	-13.01

Table 4 Calculated elastic moduli (Bulk modulus (B), Young's modulus (Y), and Shear modulus (G) all in GPa unit) and Poisson's ratio (ν) (unitless) under different unidirectional pressure (in GPa units). Here, the subscripts V, R and H represent Voigt, Reuss and Hill assumptions respectively.

P	B_V	B_R	B_H	Y_V	Y_R	Y_H	G_V	G_R	G_H	ν_V	ν_R	ν_H
0	34.171	26.067	30.119	63.406	27.146	45.921	26.625	10.233	18.429	0.19074	0.32643	0.24589
10	59.384	41.197	50.291	90.613	67.677	79.168	36.371	27.596	31.983	0.24569	0.22621	0.23763
12	66.34	42.744	54.542	91.177	67.057	79.182	35.87	27.071	31.471	0.27094	0.23853	0.25804
20	85.458	68.677	77.068	102.74	79.334	91.042	39.527	30.339	34.933	0.29963	0.30747	0.30311
30	99.032	93.485	96.259	106.13	79.365	92.894	40.157	29.21	34.684	0.32139	0.35851	0.33916
40	103.42	99.311	101.37	106.93	77.512	92.424	40.271	28.291	34.281	0.32767	0.36992	0.34803
50	65.593	-118.29	-26.349	93.411	601.82	-5549.5	36.99	128.16	82.574	0.26265	1.34790	-34.603

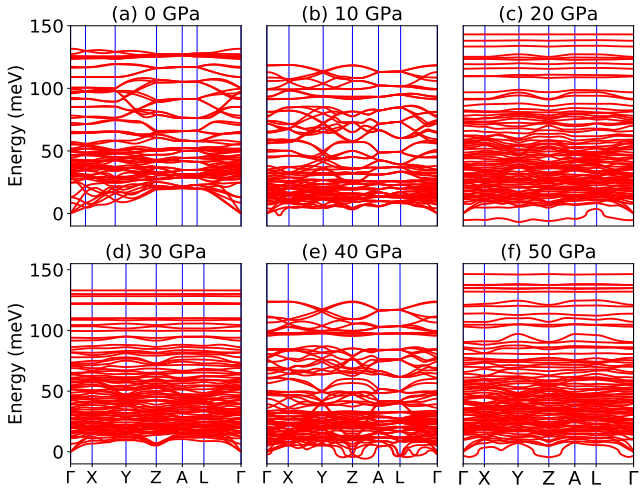

Fig. 3 Phonon dispersion curve of Na_2SiO_3 under (a) 0 GPa, (b) 10 GPa, (c) 20 GPa, (d) 30 GPa, (e) 40 GPa, (f) 50 GPa.

dispersion while the bottom of the conduction bands (CBs) have large dispersion for all different compressive pressures (see Fig.4). This is in good agreement with the electronic band structure result reported by F.Lui *et al.*[59] using ab initio total-energy and force calculations within the local density approximation (LDA) via a preconditioned conjugate gradient algorithm. From our calculation, at P=0 GPa [see fig. 4(a)], the highest energy of the valence band is at the Z point, and

Table 5 Calculated eigenvalues of stiffness matrix (in GPa units) calculated from elastic constants under different unidirectional pressures.

P	λ_1	λ_2	λ_3	λ_4	λ_5	λ_6
0	5.7103	19.843	28.63	47.31	50.672	112.62
10	16.694	32.253	41.275	54.111	90.336	196.98
12	23.039	25.862	32.821	54.016	93.228	217.47
20	16.984	27.313	54.458	56.227	123.93	271.14
30	15.739	20.84	60.16	70.957	131.56	302.32
40	15.909	17.629	63.062	77.369	127.3	314.75
50	-20.633	21.085	44.627	54.416	120.81	240.59

the lowest energy of the conduction band is at the Γ point, and with an indirect (Z to Γ points) band gap of 2.97 eV. Experimentally, Sigel[60] had reported a band gap of 6 eV for silicate glasses. It is well known that the PBE-GGA density functional theory calculations usually underestimates the band gap. An indirect (Z to Γ points) band gap was reported by F.Lui *et al.*[59] but with a band gap value of 4 eV. Ching *et al.*[18] had reported band gap values of 6.46 eV with $\alpha = \frac{2}{3}$ and 9.98 eV with α = 1.0 and concluded that the band gap of Na_2SiO_3 was very dependent on the exchange parameter used. In this work, we have done elctronic band structure calculation under compressive pressures in the pressure range of 0-50 GPa with a difference of 10 GPa. It is found that the highest energy point of the valence band changes with pressure while the bottom of the conduction band is at Γ point for all different pressures,

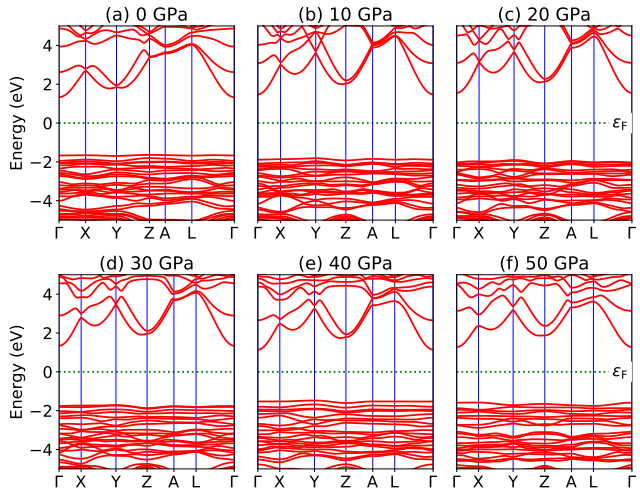

Fig. 4 Calculated band structure (a)P=0 GPa, (b) P=10 GPa, (c) P=20 GPa, (d) P=30 GPa, (e) P=40 GPa and (e) P=50 GPa.

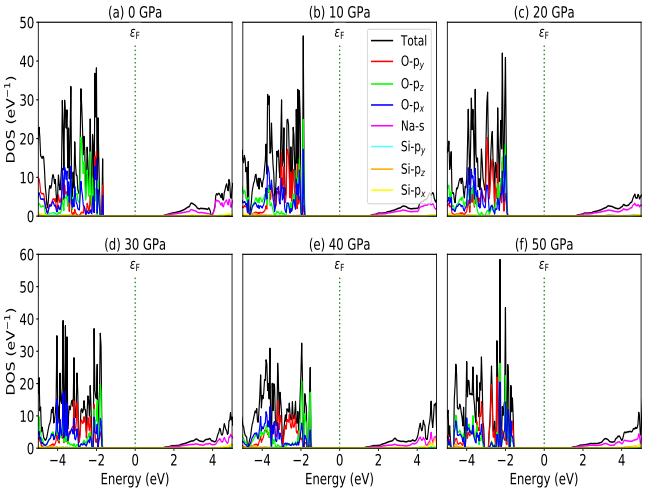

Fig. 5 Partial density of states (a) P=0 GPa, (b) P=10 GPa, (c) P=20 GPa, (d) P=30 GPa, (e) P=40 GPa and (e) P=50 GPa.

see fig. 4(a-f). It is obvious that the application of pressure changes the lattice parameters and so for the reason, average distance between electron or hole. This in turn changes the magnitude of the electron-hole ions potential. This change in the potential is significant as it plays an important role in determining the band gap at the Brillouin zone. In this work, we have found that the band gap fluctuate with the application of pressure. Initially, the band gap increases upto 20 GPa, and from 20 GPa-40 GPa the band gap decreases linearly. From 40 GPa-50 GPa, the band gap starts to increase again (see fig. 6 for variation of band gap with the application of pressure). Obviously, the band gap should decrease with increasing applied pressure but, from our calculation, we can clarify that

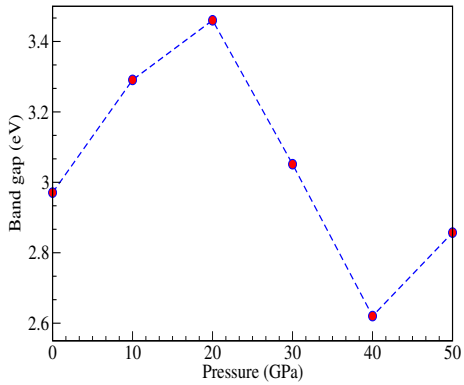

Fig. 6 Calculated band gap (in eV) versus pressure (in GPa) for Na_2SiO_3. Here, the red dots represent the corresponding band gaps at 0, 10, 20, 30, 40, 50 GPa.

the variation in band gap with the application of pressure does not have specific trend followed (i.e., there is a rise and fall in the band gap value when the amount of applied pressure is increasing). This might be due to the nature of the material that we are being investigating.

The calculated PDOS of Na_2SiO_3 at 0 GPa, 10 GPa, 20 GPa, 30 GPa, 40 GPa and 50 GPa are shown in Fig. 5 (a), (b), (c), (d), (e) and (f), respectively. The Fermi level (ε_F) is set at 0 eV which lies between the valence band and the conduction band. At 0 GPa, the energy states around the top of the valence band is mainly contributed by the states O-2p_x and O-2p_y orbitals. And, the valence band electronic states are mainly distributed in the energy range from -3.8 eV to -1.8 eV owing the hybridization of O-2p_x, O-2p_y, O-2p_z and Si-3p_x. The energy states around the bottom of the conduction band is composed mainly by the Na-3s orbitals and also, we could find a slight contribution from Si-3p_x orbitals. With the application of pressure, the main contributors of the energy state at the top of the valence band changes i.e., from the state O-2p_y to O-2p_z till it reaches 40 GPa [see Fig. 5 (b, c, d and e)] while, the energy states which contributed the bottom of the conduction band remain consistent. Clearly, we could find an overall shifting of both the valence band and conduction band when pressure is increasing. At 10 and 20 GPa's both the top of valence band and the bottom of conduction band shifted away from the Fermi level (ε_F). Therefore, the band gap is large. Hence, light of a higher frequency and lower wavelength would be absorbed. Between 30-50 GPa, we observed the reverse characteristics where both the top of valence band and the bottom of conduction band shifted towards the Fermi level (ε_F). As a results, there is a reduction in band gap and therefore, the light absorption in the visible range might be improved.

3.4 Optical properties

The optical properties of a material define how the material interacts with the electro-magnetic radiation.[61] So, detail study of the optical properties is crucial in many industrial and other scientific applications such as heat transfer, contactless temperature measurement, laser technology, optics industry for the productions of mirrors, lenses and optical windows, photovoltaic industry, the aerospace industry and so on.[62,63] Therefore, we have studied the optical properties of Na_2SiO_3 at different compressive pressures by calculating the dielectric constant (ε), absorption coefficient (α) and refractive index (η) as a function of the photon energy(eV). We have calculated the optical properties of Na_2SiO_3 in terms of complex dielectric function which is closely related to the interaction between the photons (electromagnetic radiation) and the electrons (atoms), therefore it is represented by both the real and the imaginary parts given by[64–67]:

$$\varepsilon = \varepsilon_1 + i\varepsilon_2 \tag{3}$$

where ε_1 and ε_2 are the real part and imaginary part of the dielectric constant, respectively. The above equation is mainly connected with the electronic structures and determines the linear response of the materials to electromagnetic radiations. The imaginary part (ε_2) is related to the electronic band and represent the optical absoption in the crystal and is given by[64–67]:

$$\varepsilon_2(\omega) = \frac{\hbar^2 e^2}{\pi m^2 \omega^2} \sum_{nn'} \int_k d^3k \left| \langle \vec{k}n|\vec{p}|\vec{k}n'\rangle \right|^2 \times \left[1 - f(\vec{k}n)\right] \delta(E_{\vec{k}n} - E_{\vec{k}n'} - \hbar\omega) \tag{4}$$

where $\vec{p}$ is the momentum operator, $|\vec{k}n\rangle$ is the eigenfunction of the eigenvalue $E_{\vec{k}n}$ and $f(\vec{k}n)$ is the Fermi distribution function. The real part (ε_1) is evaluated from the imaginary part (ε_2) using the Kramers-Kronig transformation[68] which is given by:

$$\varepsilon_1(\omega) = 1 + \frac{2}{\pi} \int_0^\infty \frac{\varepsilon_2(\omega')\omega' d\omega'}{\omega'^2 - \omega^2} \tag{5}$$

The optical constant, the refractive index (η) can be computed from the complex dielectric function (ε_1). The absorption coefficient(α) and the refractive index(η) which are the optical properties related to the dielectric function and are given by:

$$\alpha(\omega) = \frac{2\omega\kappa(\omega)}{c} \tag{6}$$

where $\kappa(\omega)$ is the extinction coefficient related to the imaginary part of the complex refactive index.

$$\eta(\omega) = \sqrt{\frac{(\varepsilon_1^2 + \varepsilon_2^2)^{\frac{1}{2}} + \varepsilon_1}{2}} \tag{7}$$

Table 6 Calculated static real part of the dielectric constant $\varepsilon_1(0)$ and static refractive indices $\eta(0)$ along x, y, z-axes under 0, 10, 20, 30, 40 and 50 GPa pressures.

P	$\varepsilon_1^x(0)$	$\varepsilon_1^y(0)$	$\varepsilon_1^z(0)$	$\eta^x(0)$	$\eta^y(0)$	$\eta^z(0)$
0	1.07	1.18	1.04	1.03	1.08	1.01
10	1.08	1.04	1.20	1.04	1.02	1.09
20	1.05	1.03	1.16	1.02	1.01	1.07
30	1.05	1.05	1.24	1.02	1.02	1.10
40	1.06	1.03	1.36	1.02	1.01	1.16
50	1.11	1.08	1.18	1.05	1.03	1.08

The presence of discrete spikes in the electronic density of states influence the optical properties. The real part(ε_1) and imaginary part(ε_2) of dielectric constant as a function of the photon energy up to 10 eV along x, y, z-axes under P=0, 10, 20, 30, 40, 50 GPa's are presented in Fig. 7(a,b). The calculated static real dielectric function $\varepsilon_1(0)$ (at E=0.0 eV) along x, y, z-axes are presented in Table 6. The real dielectric function ε_1 shows anisotropic behaviour up to 10 eV, beyond 10 eV the values of ε_1 is $\sim$1 arb. unit under different applied pressures along different axes exhibiting negligible effect of pressure on the ε_1 for high values of the photon energy. Meanwhile, along x-axis one could find one prominent peak for each different pressures, as shown in Fig. 7(a) (top). For 0 GPa the peak point is at around 5.0 eV with a value of 1.3 arb. unit. The peak points shifted to the higher energy region as pressure is increasing till it reaches 20 GPa and from 30 GPa the peak points shifted back to the lower energy region till the pressure reaches 50 GPa where the peak point is at around 2.85 eV with a peak value of 1.24 arb. unit. The value of ε_1^x goes to a lower value after reaching the maximum point. The minimum points for all different pressures are in the energy region where the photon energy is at 5 eV-6.2 eV with the minimum value in the range of 0.65-0.80 arb. unit. However, along y-axis, as shown in Fig. 7(a) (middle), we can notice two prominent peak points for 0 GPa where the first peak is at around 2.85 eV and the second peak is at around 4.8 eV with peak values of $\sim$1.4 and $\sim$1.3 arb. units, respectively, and as the photon energy is increasing ε_1^y drops below 0.5 arb. unit at around 6 eV. The peak value as well as the lowest value of ε_1^y at 0 GPa are comparatively high and low, respectively, when comparing with the peak value and the lowest value at all other pressures that are being applied within the same energy range. This indicates that along y-axis, the photon energy might have the greatest effect on the refractive index when pressure is at 0 GPa. Considering from the second peak, one can note that ε_1^y shows similar behaviour as that in the case of ε_1^x where the peak points shifted to the higher photon energy region and goes back to the lower photon energy when pressure is increasing. Along z-axis, as shown in Fig. 7(a) (bottom), the value of ε_1^z at 0 GPa almost remains unity throughout the en-

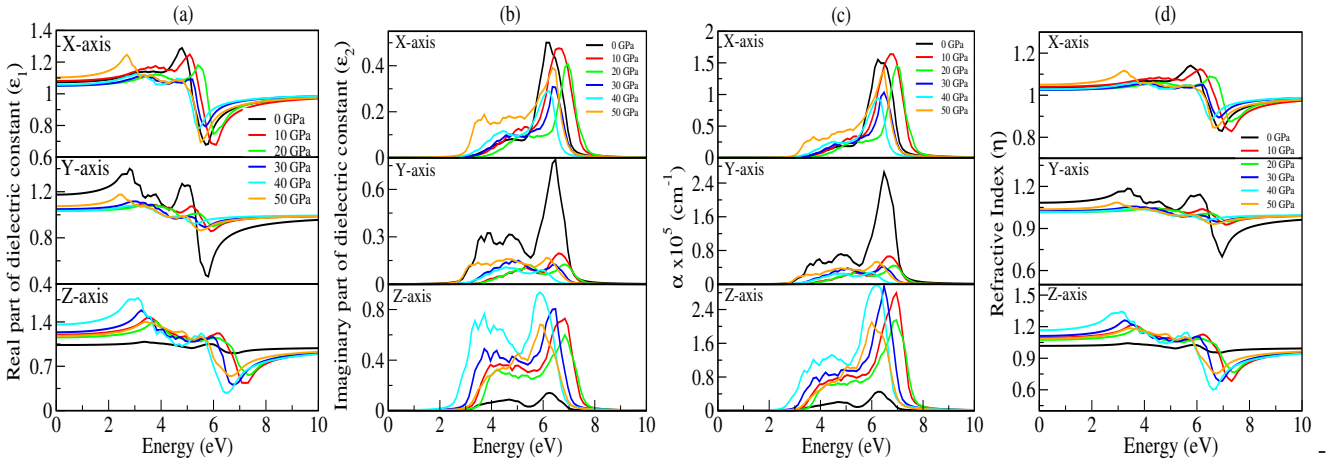

Fig. 7 Optical parameters as a function of the photon energy(in eV) under 0, 10, 20, 30, 40, and 50 GPa pressures: (a) Real part of dielectric function(ε_1), (b) Imaginary part of dielectric function(ε_2), (c) Absorption coefficient(α) and (d) Refractive index(η).

ergy ranges, it has a maximum peak value at around 6 eV with a value of ∼1.05 arb. unit. As pressure is increasing the peak points are shifted to the lower energy region within the energy range of 3.0 eV-4.0 eV. At 40 GPa one could find the highest peak for this axis which is at around 3.0 eV with a value of ∼1.75 arb. unit. The imaginary part of the dielectric constant ε_2 is interconnected with the dielectric losses and also, corresponds to the inter-band transition between the valence band and conduction band. It is highly correlated with the optical absorption (α) of a materials [see Fig. 7(c)]. Plot of imaginary part of dielectric constant (ε_2) as a function of photon is shown in Fig. 7(b). Along x and y-axes, one can notice that the peak points of ε_2^x and ε_2^y [see 7(b)(top and middle)] are shifted to the higher photon energy region when pressure is increasing till the pressure reaches 20 GPa but above this the peak points shifted back towards the lower energy region which is very similar with the one we obtained in the real part. However, when analyzing our calculated data for ε_2 along the z-axis, it clearly shows that within the same energy range the ε_2^z has much higher value when comparing with ε_2^x and ε_2^y, except at 0 GPa. This is due to the fact that the pressure is applied along the z-axis. We have measured absorption coefficients (α) along x, y, z-axes as a function of incident photon energy shown in Fig. 7(c). Here, we can find a very strong optical absorption along x, y, z-axes (α^x, α^y, α^z) under different pressures within the energy range of 0-10 eV. The most active region is found in between 2.5 eV to 8.0 eV. The absorption spectra is highly anisotropic in nature. Our main concerns is to observe the variation of absorption spectra under applied pressure for its potential application in opto-electronic devices. Our results of absorption spectra is very interesting because it falls within UV-Vis range. Referring to Fig. 7(c)(bottom), the absorption spectra peaks have shown blue shift up to 20 GPa pressure after that there is a small red shift as compared to the one at 0 GPa. The intensity of absorption spectra increases as we keep increasing pressure up to 40 GPa. The minimum threshold energy is found to be 2.5 eV which is corresponds to an optical band gap in good agreement with electronic band gap at 40 GPa [Fig. 7(c)(bottom)]. We have observed four prominent peaks at 3.2 eV, 3.8 eV, 4.5 eV and 6 eV. The optical band gap is result of first direct electron transition from top of the valence band (O-p_z) to the bottom of the conduction band (Na-s) along Γ-symmetry. The first peak at 3.2 eV is a result of transition from third band of valence region to bottom of conduction band (Γ-symmetry). The second peak at 3.8 eV is a probability transition from top of valence band to bottom of conduction band along Z-symmetry point. The third peak at 4.5 eV is due to the outcome of the transition from second band of valence region to first band of conduction region along x-symmetry. The last peak at 6 eV having the maximum intensity is due to third band of valence region to third band of conduction region along x-symmetry. Interestingly, the maximum intensity peaks shifted towards the higher energy on increasing the pressure for x- and y-axes which is contrary to the absorption spectra peak measured along z-axis. This discrepancy is due to the tensile strain along x- and y-axes while the compressive strain is experienced by the atom along z-axis on application of unidirectional pressure (along z-axis). The calculated spectra of refractive indices (η) along x, y, z-axes are presented in Fig. 7(d). The static refractive indices $\eta_{x,y,z}(0)$ are given in Table 6. Clearly, all the values are close to unity at 0 eV indicating that our system Na_2Si0_3 is transparent in nature. Recently, Baral *et al.*[69] had reported that the high refractive index of $(Na_2O)_x(SiO_2)_{1-x}$ when sodium oxide concentration was increased. Using the orthogonalized linear combination of atomic orbitals (OLCAO) method in the

VASP-relaxed structures he reported η value in the range of 1.415-1.530 when concentration was x=0-0.5. On analysing the variation of refractive indices (η) with respect to the incident photon energy (eV) under unidirectional pressure along the z-axis, one can find the change in refractive index is almost negligible along the x- and y-axes up to around 5.5 eV even when the pressure reaches 50 GPa [see Fig. 7(d) (top and middle)]. However, referring to Fig. 7(d)(bottom), along the z-axis we have noticed an isotropic behaviour. The refractive indices start increasing at around 3 eV as pressure escalates compare to the one at 0 GPa where the value almost remains unity throughout the whole incident photon energy. Meanwhile, above 6 eV the values of all the refractive indices along (i.e., along x, y, z) falls below 1 up to around 10 eV [see Fig. 7(d)]. This seems physically not possible as refractive index below 1 occurs only when the speed of light is exceeded by phase velocity of electro-magnetic wave (v_p >c). In addition, this phenomenon arises due to the presence of plasmonic vibration.

3.5 Piezoelectric properties

It is well-known that the piezoelectric properties of a materials arise as a result of the atomic scale polarization which could be due to the application of mechanical stress.[70] Study of piezoelectric properties of a materials has become an interesting topic among the researchers as those materials have a industrial applications such as; as actuators, sensors, microphones and so on, also it has an application in medical devices for monitoring heartbeats and breathing.[71–78] To our knowledge the insight study of piezoelectric properties of a materials are usually based on the study of piezoelectric tensors (d_{kij}).[79,80] Interestingly, in this section we are going to discuss about the piezoelectric properties of glass-like Na_2SiO_3 by calculating the total Cartesian polarization under different compressive unidirectional pressures as shown in Table 7. Our calculation is simply based on the modern theory of polarization where the spontaneous polarization of a materials are calculated to understand about its ferroelectric property. Since quartz (SiO_2) are naturally occurring single crystalline piezoelectric materials, therefore, our system Na_2SiO_3 has a possibility of showing piezoelectric property. In modern theory of polarization, polarization of a materials are divided into two parts; electronic and ionic parts. The contribution of electronic part to polarization is given as[81]:

$$P_e = \frac{-2|e|i}{(2\pi)^3}\int_A dk_\perp \sum_{n=1}^{M}\int_0^{G_\parallel}\langle U_{k,n}|\frac{\partial}{\partial k_\parallel}|U_{k,n}\rangle\, dk_\parallel \qquad (8)$$

here, the summation runs over occupied bands, and $k_\parallel$ is parallel to the direction of polarization, and $G_\parallel$ is a reciprocal lattice vector in the same direction. The states $|U_{k,n}\rangle$ are the cell-periodic parts of the Bloch functions, $\psi_{k,n}$=$U_{n,k}(r)e^{ik.r}$. The electronic polarization part is simply calculated by classical electrostatic sum of point charges given as:

$$P_i = \frac{|e|}{\Omega}\sum_\nu Z^\nu_{ion} r^\nu \qquad (9)$$

where the summation runs over all the ions in the unit cell, and Z^ν_{ion} and r^ν are the valence charge and position vector of atom ν, and Ω is the volume of unit cell.
The total Cartesian polarization (P_t(c)) is calculated by taking the product of total fractional polarization (P_t) and polarization quantum (P_q), i.e.,

$$P_t(c) = P_t \cdot P_q \qquad (10)$$

where P_t=P_e+P_i is the sum of electronic and ionic polarization parts and P^j_q=$\frac{|e|R^j}{\Omega}$ is the polarization quantum, here, $|e|$ is electronic charge, R^j is lattice vector j and Ω unit cell volume. Our calculated total Cartesian polarization in Cm^{-2} unit under the application of different compressive unidirectional pressures are given in Table 7. From our calculation, one can find that at 0 GPa the Cartesian polarization is maximum along the z-direction with a value of $\sim$ 0.1 Cm^{-2}. This indicates that Na_2SiO_3 has shown some properties of ferroelectricity. However, when pressure is applied along the z-axis, it is obvious that one will notice a compressive stress along the z-axis while tensile stress will be observed along both x- and y-axes. This structural changes with pressure will patently distort the negative cloud of electrons around positive atomic nuclei. This slight separation will result in an electric field between them, and consequently polarization is created which can be manipulated to give novel piezoelectric properties. Our biggest concerns is to obtain the Cartesian polarization of Na_2SiO_3 for its potential application in piezoelectric materials. Interestingly, from Table 7 we have observed that the maximum polarization axis changes from z to y-axes as pressure increases from 0 GPa to 40 GPa. At 50 GPa the Cartesian polarization has its highest value along the x-axis. The calculated Cartesian polarization for 10, 20, 30, 40 and 50 GPa's are $\sim$ 0.041, 0.063, 0.076, 0.065 and 0.018 (in Cm^{-2}) which are fairly low. Therefore, to use Na_2SiO_3 in practical ferroelectric and piezoelectric devices a rigorous research is necessary which could further enhance its polarizability.

4 Conclusions

In summary, we have studied the properties of sodium silicate (Na_2SiO_3) by using DFT calculations under different unidirectional compressive pressures. Our findings revealed that Na_2SiO_3 is a stable structure which shows mechanical stability upto 40 GPa. And at 12 GPa, our system experiences

Table 7 Calculated total cartesian polarization P_t(c) in Cm^{-2} along x, y, z-axes under different compressive unidirectional pressure.

P	0	10	20	30	40	50
x	-2.97064990×10^{-3}	-2.66488487×10^{-2}	2.36226850×10^{-2}	-7.18990850×10^{-3}	-9.0549006×10^{-3}	1.77675552×10^{-2}
y	-2.29594955×10^{-2}	4.11457135×10^{-2}	6.31891403×10^{-2}	7.57134265×10^{-2}	6.49859613×10^{-2}	-6.33370486×10^{-2}
z	1.00901047×10^{-1}	1.64564653×10^{-2}	8.47809484×10^{-3}	-5.85834073×10^{-3}	-3.35035488×10^{-3}	1.39032451×10^{-3}

structural phase transition from orthorhombic C$mc2_1$ to lower primitive symmetry of triclinic P1 structure. Also, at 50 GPa Na_2SiO_3 is found to have an auxetic materials property which opens up its potential applications in the field of biomedical and other electronic devices. Interestingly, Na_2SiO_3 is found to have its optical absorbance falls within UV-Vis range. The value of $\eta^{x,y,z}(0)\sim1$ has revealed that Na_2SiO_3 is transparent in nature. Therefore, it is a promising materials for optoelectronic devices.

5 Acknowledgement

D. P. Rai acknowledges Govt. of India, Ministry of Science and Technology, Department of Science & Technology (International Bilateral Cooperation Division) for supporting Indo-Uzbek joint project via Sanction No. INT/UZBEK/P-02.

References

1 L.-g. Liu, *Geophys. Res. Lett.*, 1987, **14**, 1079–1082.
2 J. M. D. Coey, *Mössbauer Spectroscopy Applied to Inorganic Chemistry*, Springer US, Boston, MA, 1984, pp. 443–509.
3 L. Zhu, Y. R. Zeng, J. Wen, L. Li and T. M. Cheng, *Electrochim. Acta*, 2018, **292**, 190–198.
4 Y. Ren, Y. Zhang, Y. Gu and Q. Zeng, *Prog. Org. Coatings*, 2017, **112**, 225–233.
5 M. Lancry, E. Régnier and B. Poumellec, *Prog. Mater. Sci.*, 2012, **57**, 63–94.
6 S. Kaya, M. Cresswell and A. R. Boccaccini, *Mater. Sci. Eng. C*, 2018, **83**, 99–107.
7 E. Borsella, E. Cattaruzza, G. De Marchi, F. Gonella, G. Mattei, P. Mazzoldi, A. Quaranta, G. Battaglin and R. Polloni, *J. Non. Cryst. Solids*, 1999, **245**, 122–128.
8 J. O. Bockris, J. D. Mackenzie and J. A. Kitchener, *Trans. Faraday Soc.*, 1955, **51**, 1734.
9 C. A. Faick and A. N. Finn, *J. Am. Ceram. Soc.*, 1931, **14**, 518–528.
10 L. SHARTSIS, S. SPINNER and W. CAPPS, *J. Am. Ceram. Soc.*, 1952, **35**, 155–160.
11 T. Uchino, M. Iwasaki, T. Sakka and Y. Ogata, *J. Phys. Chem.*, 1991, **95**, 5455–5462.
12 A. K. Varshneya and J. C. Mauro, *Fundam. Inorg. Glas.*, Elsevier, 2019, pp. 1–18.
13 J. T. Randall, H. P. Rooksby and B. S. Cooper, *Zeitschrift für Krist. - Cryst. Mater.*, 1930, **75**, 196–214.
14 W. H. Zachariasen, *J. Am. Chem. Soc.*, 1932, **54**, 3841–3851.
15 I. Farnan, *Nature*, 1997, **390**, 14–15.
16 K. Baral, A. Li and W.-Y. Ching, *J. Phys. Chem. A*, 2017, **121**, 7697–7708.
17 S. Kikuchi, N. Koga, H. Seino and S. Ohno, *J. Nucl. Sci. Technol.*, 2016, **53**, 682–691.
18 W. Y. Ching, R. A. Murray, D. J. Lam and B. W. Veal, *Phys. Rev. B*, 1983, **28**, 4724–4735.
19 A. Grund and M. Pizy, *Acta Crystallogr.*, 1952, **5**, 837–840.
20 D. D. Le Pevelen, *Encycl. Spectrosc. Spectrom.*, 2010, pp. 2559–2576.
21 P. Richet, B. O. Mysen and D. Andrault, *Phys. Chem. Miner.*, 1996, **23**, 157–172.
22 G. Greaves, *J. Non. Cryst. Solids*, 1985, **71**, 203–217.
23 Y. Cao, A. N. Cormack, A. G. Clare, B. Bachra, A. C. Wright, R. N. Sinclair and A. C. Hannon, *J. Non. Cryst. Solids*, 1994, **177**, 317–323.
24 D. W. Matson, S. K. Sharma and J. A. Philpotts, *J. Non. Cryst. Solids*, 1983, **58**, 323–352.
25 H. Maekawa, T. Maekawa, K. Kawamura and T. Yokokawa, *J. Non. Cryst. Solids*, 1991, **127**, 53–64.
26 G. N. Greaves, S. J. Gurman, C. R. A. Catlow, A. V. Chadwick, S. Houde-Walter, C. M. B. Henderson and B. R. Dobson, *Philos. Mag. A*, 1991, **64**, 1059–1072.
27 M. G. Mortuza, R. Dupree and D. Holland, *J. Non. Cryst. Solids*, 2001, **281**, 108–116.
28 L. Olivier, X. Yuan, A. N. Cormack and C. Jäger, J. Non. Cryst. Solids, 2001, pp. 53–66.
29 A. Meyer, J. Horbach, W. Kob, F. Kargl and H. Schober, *Phys. Rev. Lett.*, 2004, **93**, year.
30 B. Gee and H. Eckert, *J. Phys. Chem.*, 1996, **100**, 3705–3712.
31 G. N. Greaves, A. Fontaine, P. Lagarde, D. Raoux and S. J. Gurman, *Nature*, 1981, **293**, 611–616.
32 Y. Kowada and D. E. Ellis, *Adv. Quantum Chem.*, 1998, vol. 29, pp. 233–251.
33 A. Bunde, M. Ingram, P. Maass and K. Ngai, *J. Non. Cryst. Solids*, 1991, **131-133**, 1109–1112.
34 R. L. McGreevy and L. Pusztai, *Mol. Simul.*, 1988, **1**, 359–367.
35 S. Ispas, M. Benoit, P. Jund and R. Jullien, *Phys. Rev. B*, 2001, **64**, 214206.
36 Z. Q. Hu, A. M. Wang and H. F. Zhang, *Mod. Inorg. Synth. Chem. Second Ed.*, Elsevier, 2017, pp. 641–667.
37 S. Smidstrup, T. Markussen, P. Vancraeyveld, J. Wellendorff, J. Schneider, T. Gunst, B. Verstichel, D. Stradi, P. A. Khomyakov, U. G. Vej-Hansen, M.-E. Lee, S. T. Chill, F. Rasmussen, G. Penazzi, F. Corsetti, A. Ojanperä, K. Jensen, M. L. N. Palsgaard, U. Martinez, A. Blom, M. Brandbyge and K. Stokbro, *J. Phys. Condens. Matter*, 2020, **32**, 015901.
38 S. Smidstrup, D. Stradi, J. Wellendorff, P. A. Khomyakov, U. G. Vej-Hansen, M.-E. Lee, T. Ghosh, E. Jónsson, H. Jónsson and K. Stokbro, *Phys. Rev. B*, 2017, **96**, 195309.
39 M. Schlipf and F. Gygi, *Comput. Phys. Commun.*, 2015, **196**, 36–44.
40 J. P. Perdew, K. Burke and M. Ernzerhof, *Phys. Rev. Lett.*, 1996, **77**, 3865–3868.
41 D. C. Liu and J. Nocedal, *Math. Program.*, 1989, **45**, 503–528.
42 S. H. Hahn, J. Rimsza, L. Criscenti, W. Sun, L. Deng, J. Du, T. Liang, S. B. Sinnott and A. C. T. van Duin, *J. Phys. Chem. C*, 2018, **122**, 19613–19624.
43 A. Pedone, G. Malavasi, A. N. Cormack, U. Segre and M. C. Menziani, *Chem. Mater.*, 2007, **19**, 3144–3154.
44 M. van Setten, M. Giantomassi, E. Bousquet, M. Verstraete, D. Hamann,

X. Gonze and G.-M. Rignanese, *Comput. Phys. Commun.*, 2018, **226**, 39–54.
45 H. J. Monkhorst and J. D. Pack, *Phys. Rev. B*, 1976, **13**, 5188–5192.
46 C. Cuautli, I. Romero-Ibarra, J. Vazquez-Arenas and M. Galvan, *Fuel*, 2021, **298**, 120840.
47 D. Belmonte, C. Gatti, G. Ottonello, P. Richet and M. V. Zuccolini, *J. Phys. Chem. A*, 2016, **120**, year.
48 W. S. McDonald and D. W. J. Cruickshank, *Acta Crystallogr.*, 1967, **22**, 37–43.
49 F. Mouhat and F.-X. Coudert, *Phys. Rev. B*, 2014, **90**, 224104.
50 Q. Guo, K. C. Lau and R. Pandey, *J. Phys. Chem. C*, 2019, **123**, 4674–4681.
51 *Voigt, W. (1928) Lehrbuch der Kristallphysik. Teubner Verlag, Leipzig. - References - Scientific Research Publishing*.
52 A. Reuss, *ZAMM âĂŘ J. Appl. Math. Mech. / Zeitschrift für Angew. Math. und Mech.*, 1929, **9**, 49–58.
53 R. Hill, *Proc. Phys. Soc. Sect. A*, 1952, **65**, 349–354.
54 S. Chokka and K. Traipanya, *SURANAREE J. Sci. Technol.*, 2017, **24**, 407–414.
55 M. Sanami, *PhD thesis*, 2015.
56 E. P. HADJIGEORGIOU and G. E. STAVROULAKIS, *Comput. Methods Sci. Technol.*, 2004, **10**, 147–160.
57 S. Farhangdoust, S. M. Aghaei, M. Amirahmadi, N. Pala and A. Mehrabi, Sensors Smart Struct. Technol. Civil, Mech. Aerosp. Syst. 2020, 2020, p. 36.
58 T. Fey, F. Eichhorn, G. Han, K. Ebert, M. Wegener, A. Roosen, K. I. Kakimoto and P. Greil, *Smart Mater. Struct.*, 2015, **25**, 015017.
59 F. Liu, S. H. Garofalini, R. D. King-Smith and D. Vanderbilt, *Chem. Phys. Lett.*, 1993, **215**, 401–404.
60 G. H. SIGEL, *TREATISE Mater. Sci. Technol.*, ACADEMIC PRESS, INC., 1977, vol. 12, pp. 5–89.
61 V. Sudarsan, *Funct. Mater.*, Elsevier, 2012, pp. 285–322.
62 L. Barnett, *Dev. Agric. Eng.*, Elsevier, 1986, vol. 8, pp. 48–55.
63 A. K. Varshneya and J. C. Mauro, *Dev. Agric. Eng.*, Elsevier, 1986, vol. 8, pp. 48–55.
64 C. Ambrosch-Draxl and J. O. Sofo, *Comput. Phys. Commun.*, 2006, **175**, 1–14.
65 D. P. Rai, T. V. Vu, A. Laref, M. P. Ghimire, P. K. Patra and S. Srivastava, *Nano-Structures and Nano-Objects*, 2020, **21**, 100404.
66 B. Chettri, P. K. Patra, Lalmuanchhana, Lalhriatzuala, S. Verma, B. K. Rao, M. L. Verma, V. Thakur, N. Kumar, N. N. Hieu and D. P. Rai, *Int. J. Quantum Chem.*, 2021, **121**, e26680.
67 B. Chettri, P. K. Patra, T. V. Vu, C. Q. Nguyen, Lalrinkima, A. Yaya, K. O. Obodo, N. T. T. Tran, A. Laref and D. P. Rai, *Phys. E Low-Dimensional Syst. Nanostructures*, 2021, **126**, 114436.
68 P. C. Martin, *Phys. Rev.*, 1967, **161**, 143–155.
69 K. Baral and W.-Y. Ching, *J. Appl. Phys.*, 2017, **121**, 245103.
70 Y. J. Lu, Z. F. Shi, C. X. Shan and D. Z. Shen, *Nanoscale Semicond. Lasers*, Elsevier, 2019, pp. 75–108.
71 D. Damjanovic and R. E. Newnham, *J. Intell. Mater. Syst. Struct.*, 1992, **3**, 190–208.
72 J. Nuffer and T. Bein, *Glob. Symp. Innov. Solut. Adv. Transp. Ind.*, 2006, 4–6.
73 E. Aksel and J. L. Jones, *Advances in lead-free piezoelectric materials for sensors and actuators*, 2010.
74 M. T. Chorsi, E. J. Curry, H. T. Chorsi, R. Das, J. Baroody, P. K. Purohit, H. Ilies and T. D. Nguyen, *Adv. Mater.*, 2019, **31**, 1802084.
75 G. Gautschi, *Piezoelectric Sensorics*, Springer Berlin Heidelberg, Berlin, Heidelberg, 2002, pp. 73–91.
76 S. Zhang and F. Yu, *J. Am. Ceram. Soc.*, 2011, **94**, 3153–3170.
77 Y. Y. Chiu, W. Y. Lin, H. Y. Wang, S. B. Huang and M. H. Wu, *Sensors Actuators, A Phys.*, 2013, **189**, 328–334.
78 A. Zaszczyńska, A. Gradys and P. Sajkiewicz, *Polymers (Basel).*, 2020, **12**, 2754.
79 P. Labéguerie, M. Harb, I. Baraille and M. Rérat, *Phys. Rev. B - Condens. Matter Mater. Phys.*, 2010, **81**, 045107.
80 X. Meng, X. Wen and G. Qin, Comput. Mater. Sci., 2010, pp. S372–S377.
81 R. D. King-Smith and D. Vanderbilt, *Phys. Rev. B*, 1993, **47**, 1651–1654.